

PAPER

Thermal design and analysis of a flexible solar array system based on shape memory polymer composites

To cite this article: Zhengxian Liu *et al* 2022 *Smart Mater. Struct.* **31** 025021

View the [article online](#) for updates and enhancements.

You may also like

- [Ground and geostationary orbital qualification of a sunlight-stimulated substrate based on shape memory polymer composite](#)
Fengfeng Li, Liwu Liu, Xin Lan et al.
- [Elastocaloric effects of carbon fabric-reinforced shape memory polymer composites](#)
Seok Bin Hong, Yongsan An and Woong-Ryeol Yu
- [Shape memory polymer composites by molding aeronautical prepregs with shape memory polymer interlayers](#)
F Quadrini, D Bellisario, L Iorio et al.

Thermal design and analysis of a flexible solar array system based on shape memory polymer composites

Zhengxian Liu¹, Sida Hao¹ , Xin Lan², Wenfeng Bian³, Liwu Liu¹, Qifeng Li¹, Zijian Fu², Yanju Liu¹  and Jinsong Leng^{2,*} 

¹ Department of Astronautical Science and Mechanics, Harbin Institute of Technology (HIT), Harbin 150001, People's Republic of China

² Centre for Composite Materials and Structures, Harbin Institute of Technology (HIT), Harbin 150080, People's Republic of China

³ Department of Civil Engineering, Harbin Institute of Technology (HIT), Weihai 264209, People's Republic of China

E-mail: lengjs@hit.edu.cn

Received 29 April 2021, revised 15 November 2021

Accepted for publication 7 December 2021

Published 31 December 2021



CrossMark

Abstract

Smart structures based on shape memory polymer composites (SMPCs) have attracted extensive attention because of their unique self-deployment behavior. This study investigated the thermal design and analysis of the SMPC flexible solar array system (SMPC-FSAS). The thermal design ensured the reliability of the deployment functionality and desirable structural temperatures. The fundamental properties of the shape-memory materials were obtained by dynamic mechanical analysis and shape fixity ratio tests. Thermal experiments, including the thermal balance test (TBT), thermal vacuum test and thermal cycle test were conducted to verify the safety and reliability of the SMPC-FSAS. Additionally, the temperature distribution of the SMPC-FSAS was simulated using numerical analysis. Notably, a geostationary satellite carrying the SMPC-FSAS was successfully launched into a geosynchronous orbit and controlled deployment was accomplished for the first time. The prediction of the numerical model was consistent with the TBT and on-orbit data, thus validating the accuracy of the numerical method. The research in this work has important reference significance for ultra-large SMPC-FSAS in the future.

Keywords: flexible solar array, shape memory polymer composites, thermal analysis, geosynchronous orbit

(Some figures may appear in colour only in the online journal)

1. Introduction

Shape memory polymers (SMPs) are a type of smart material that can be endowed with a specific shape after external stimuli (such as thermal, magnetic field, electricity, light) [1–6], and can recover to their original shape following further stimulation. SMPs are highly concerned to be applied

in the aviation, aerospace and medical industry [7–9] due to their shape memory characteristic. SMPs can be introduced into SMP composites (SMPCs) by adding fibers, particles and other reinforcing phases [10–14], thereby greatly improving the recovery force and mechanical properties of SMPs. SMPs can be used in various environments by tuning the reinforcing phase to acquire specific mechanical parameters [15–18].

In 2017, the National Aeronautics and Space Administration (NASA) successfully implemented an on-orbit demonstration of a roll-out solar array that could store and release

* Author to whom any correspondence should be addressed.

material strain energy [19]. At the same time, NASA also developed origami and inflatable structures as deployment mechanisms [20, 21]. These structures possess the advantages of light weight, high flexibility and high packaging efficiency. However, these structures often need the assistance of mechanical equipment. SMPCs can be used to deployable structures due to their shape memory performance of the materials [9, 22–24]. Simultaneously, the deployable structures based on the SMPCs have the advantages of light weight, high packaging efficiency, self-deployment, and low impact [25]. SMPCs are being widely studied as a new type of aerospace material. The prototype of the SMPC solar array substrate Mission SMS-I [7], developed by Jinsong Leng's research group, was carried on an experimental satellite in 2016. The prototype solar array substrate was bent into an ' Ω ' shape before launch and recovered to the flat state after deployment. Similarly, composite technology development [26] has introduced a new lightweight array (CLASP) based on SMPC, which is suitable for small satellites with high packaging efficiency.

Materials used in the aerospace field need to withstand a variety of extreme space environments, including space particle radiation, vacuum, extreme high and low temperatures, etc. The research on material level experiments for space environments was very limited. Leng *et al* [27] investigated the mechanical properties of the shape memory epoxy after 140 d of γ -ray irradiation, and proved that the irradiation environment had little effect on the mechanical properties of the material. Tan *et al* [28] concluded that the transient temperature and mechanical properties of the shape memory epoxy after 240 h of ultraviolet radiation or 45 thermal cycles have been improved. Xie *et al* [29] investigated the shape memory cyanate after vacuum outgassing and ultraviolet radiation exposure test and discovered that it has good durability in the space environment. The (micro-) failures under thermo-mechanical conditions are also critical in the thermal responsive structure. At present, there have been some material level tests [30–32]. However, thermal research on space deployable structures based on SMPCs is currently lacking.

In this work, the thermal design and analysis of the SMPC flexible solar array system (SMPC-FSAS) were investigated. The thermal design of the SMPC FSAS was carried out to ensure the function of the structure and the controllable temperature distribution. The dynamic mechanical analysis (DMA) was used to identify the glass transition temperature (T_g) of shape-memory materials. The shape fixity ratio of cyanate-based SMPC locking laminate (SMPC-LL) was tested at 80 °C, 100 °C, and 120 °C, respectively. The thermal balance test (TBT) of the SMPC-FSAS was conducted by simulating space heat radiation using a solar simulator. The thermal vacuum test (TVT) and thermal cycle test (TCT) were conducted by applying the obtained thermal balance temperatures. In addition, a numerical simulation was conducted to predict the temperature distribution of the SMPC-FSAS in orbit. Finally, a geosynchronous satellite carrying the SMPC-FSAS was successfully launched into a geosynchronous orbit, and the thermal data obtained in orbit were compared with the simulation and experimental data.

2. Structural description and thermal design

2.1. Structural description

The structure diagram of the SMPC-FSAS is shown in figure 1. The stowed and deployed states of the SMPC-FSAS are shown in figures 1(a) and (b) respectively. The SMPC-FSAS primarily consists of two locking mechanisms and two deployable mechanisms. The locking mechanism consists of two cyanate-based SMPC-LLs, and the locking and releasing functions are realized by transforming the shape of the cyanate-based SMPC-LL. In the locked state, the SMPC-LL assumes a flat shape (storage state), and it assumes a ' Ω ' shape (original state) after release. The deployable mechanism is composed of two epoxy-based SMPC lenticular tubes (SMPC-LTs). In the stowed state, the SMPC-LT assumes a curled shape (storage state), and it assumes a straight shape (original state) after deployment. Previous works [25, 33] have investigated the performance of the SMPC-LT and introduced the structural design of SMPC-FASA.

2.2. Thermal design

The SMPC-LL in the locking state needs to maintain a low-temperature environment to ensure the reliability of the SMPC-FSAS in the stowed state. However, the shape memory materials have a small specific heat capacity and are more sensitive to space thermal environment. In particular, the early release of the SMPC-LL affects the structural stiffness. Therefore, it is necessary to propose thermal control requirements. Table 1 presents the thermal control requirements of shape-memory materials.

The SMPC-FSAS was installed on the east board of the geostationary satellite. The geostationary orbit is a high orbit with a long orbit period. Therefore, if there are no thermal control measures, the surface temperature of an object easily increases. The parameters of shape-memory materials are listed in table 2.

For the thermal design and calculation of the on-orbit temperature, the steady-state heat balance equation is given as follows:

$$Q_a = Q_r \quad (1)$$

where Q_d is the dissipated heat, including heat flow that is conducted out and radiated out. Q_a is the absorbed heat, including heat flow from conduction, heat flow from radiation absorption and heat flow from inside.

According to Fourier's law, the conducted heat flow can be expressed the following:

$$\phi_c = -\lambda A \frac{dT}{dx} \quad (2)$$

where ϕ_c denotes conducted heat flow, λ denotes the thermal conductivity, A denotes the heat transfer area, and T denotes the surface temperature.

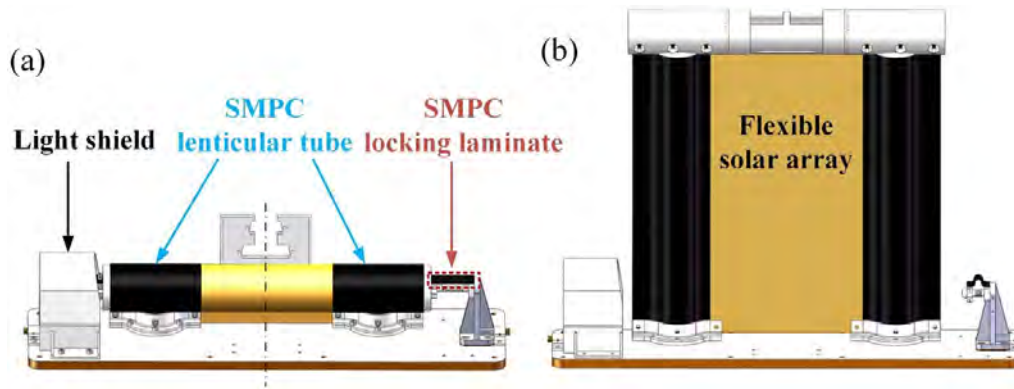


Figure 1. Structure diagram of the SMPC-FSAS: (a) stowed state of the SMPC-FSAS; (b) deployed state of the SMPC-FSAS [33].

Table 1. Thermal control requirements based on the material thermal properties of shape-memory materials.

	SMPC-LL in stowed state	SMPC-LL in deployed state	SMPC-LT in stowed state	SMPC-LT in deployed state
Thermal control temperature (°C)	<80	>173	<123	>123

Table 2. The parameters of shape-memory materials.

Material	Density (Kg m ⁻³)	Heat transfer coefficient	Specific heat capacity (J (kg·°C) ⁻¹)	Hemispherical emissivity	Solar absorptivity
Epoxy-based SMPC	1520	0.373	1.271	0.77	0.55
Cyanate-based SMPC	1720	0.481	1.198	0.75	0.711

The radiant heat flow can be described as follows:

$$\phi_r = \varepsilon\sigma(T - T_0)^4 \tag{3}$$

where ϕ_r presents radiant heat flow, ε presents the hemispheric emissivity, σ presents the Stefan–Boltzmann constant [34], and T_0 presents the background temperature.

Assuming that the temperature in space is uniform, there is no internal heat source or heat conduction. The thermal balance equation is shown in equation (4)

$$\varepsilon\sigma A(T - T_0)^4 = \alpha Q. \tag{4}$$

where α denotes the solar absorptance, and Q denotes the solar heat flow.

The thermal balance temperature of the object could be obtained from the above formula. Therefore, reducing the temperature of an object can be achieved by increasing its hemispherical emissivity and reducing its solar absorptance. According to the structural features and material properties, the thermal control design of the structure is as follows: (a) a light shield was designed and installed outside the SMPC-LL to protect it from direct sunlight from SMPC-LL and effectively prevent high temperatures from causing its premature release; (b) the silvered fluorinated ethylene propylene (F46) film [35] was pasted on the surface of the light shield and

the base. The hemispherical emissivity and solar absorptivity of the material were 0.71 and 0.07 respectively, which could effectively reduce heat conduction from other components to SMPC-LL; (c) the 5 mm polyimide heat insulation mat was designed and installed on the installed base, which effectively isolated the heat conduction between the installed base and the satellite board.

In this study, heating films were attached to either side of the SMPC-LT to provide heat. The steady-state temperature was calculated to understand the relationship between the heating power and the temperature. The calculation equation of the heating temperature of the SMPC-LT is as follows:

$$T = \frac{1}{c\rho h} \int_0^t \left[-h_{ct}(T - T_0) - \varepsilon\sigma(T - T_0)^4 - \lambda(T - T_0) + \frac{P}{A} \right] dt \tag{5}$$

where c denotes the specific heat capacity, t denotes the heating time, ρ denotes the density of the material, P denotes the heating power, h denotes the thickness of the material, and h_{ct} denotes the convective heat transfer coefficient.

Heat flow includes four parts: convection heat dissipation, radiation heat dissipation, heat conduction heat dissipation and heat transfer by the heating film. The heat flux q can be expressed as follows:

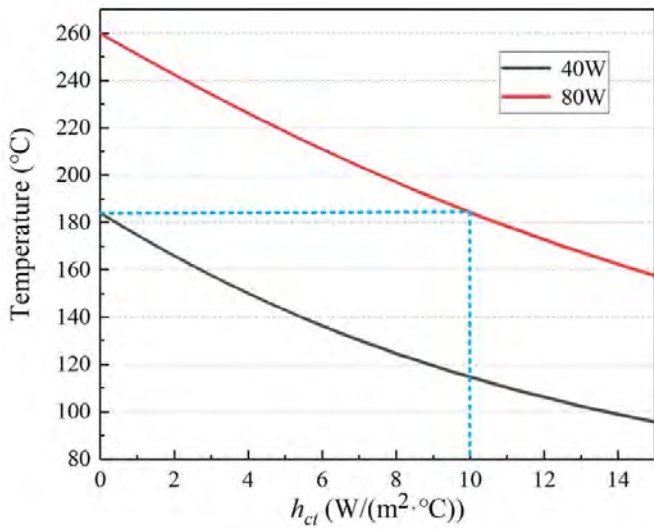


Figure 2. Relationship between the convective heat transfer coefficient and the steady-state temperature.

$$q = -(h_{ct} + \lambda)(T - T_0) - \varepsilon\sigma(T - T_0)^4 + \frac{P}{A} \quad (6)$$

when $q = 0$, the structure reaches the thermal steady state. The equation of heating power is given as follows:

$$P = A \left[(h_{ct} + \lambda)(T - T_0) + \varepsilon\sigma(T - T_0)^4 \right] \quad (7)$$

where $\sigma = 5.67 \times 10^{-8} \text{ W (m}^2 \cdot \text{K}^4)^{-1}$, $T_0 = 298.15 \text{ K}$, $A = 0.0243 \text{ mm}^2$. In this paper, the surface temperature of SMPC-LT was calculated. Because there is no convective heat transfer under vacuum conditions, the temperature during the heating process was higher than that of the ground environment. To meet the temperature requirements of the ground and vacuum at the same time, the heating film was designed with double electric circuits. The heating powers of 40 and 80 W were used in the vacuum and atmospheric environments respectively. Figure 2 plots the relationship between the convective heat transfer coefficient and the steady-state temperature. The results show that the temperature at 40 W with no convection is equivalent to that at 80 W with a convection coefficient around $10 \text{ W (m}^2 \cdot \text{°C)}^{-1}$, which represents the atmospheric environment.

3. Numerical simulation

3.1. Numerical model

Thermal simulation simulates the space thermal environmental conditions experienced by spacecraft equipment in orbit, thus can be used to effectively evaluate thermal balance temperature and functional reliability of an object. Each material in the SMPC-FSAS exhibited complex heat conduction. Thus, the finite element technique was easier to implement than the theoretical analysis. Therefore, the numerical simulation of the SMPC-FSAS was carried out by using UG NX

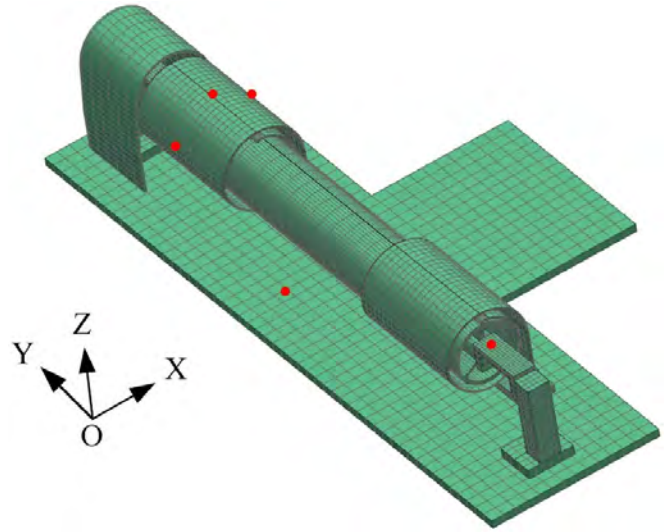


Figure 3. Simplified finite element model of the SMPC-FSAS.

software to simulate the thermal environment in orbit. The grid model and coordinate system of SMPC-FSAS are illustrated in figure 3. The five red dots represent the temperature measuring points on the surface. The measurement points were located on the base, the SMPC-LL, and at three positions on the SMPC-LT (the normal direction of the plane is X-, Z+ or X+). To satisfy the space test effect of SMPC-FSAS, the ordinary attitude and long-term facing solar attitude were simulated. For the ordinary attitude, the X+ and Z+ of the coordinate system were the same as the flight direction of the satellite and the direction facing the earth, respectively, and Y+ was determined by the right-hand rule. For the long-term facing solar attitude, the X+ and Z+ of the coordinate system faced the sun and the normal direction of the orbit, respectively, and the Y+ was determined by the right-hand rule. At this time, the flexible solar array could attain the maximum power generation voltage at this angle. The numerical simulation of the following four working conditions was carried out in this study as follows: (a) high-temperature steady-state in ordinary attitude: the heat flux was 1414 W m^{-2} (1 solar constant), and the installation surface temperature was 50 °C ; (b) low-temperature steady-state in ordinary attitude: the heat flow was 0, the installation surface temperature was -10 °C ; (c) high-temperature transient-state in ordinary attitude: the maximum heat flux was 1414 W m^{-2} , and the installation surface temperature was 50 °C ; (d) high-temperature steady-state in long-term facing solar attitude: the direction of heat flow was consistent with X-direction, the heat flux was 1414 W m^{-2} , and the installation surface temperature was 50 °C .

To evaluate the effectiveness of the light shield, this study simulated the thermal balance temperature before and after the addition of the light shield under a high-temperature environment. At the same time, we performed numerical simulations on the heating steady-state temperature of the SMPC-LTs to further understand the steady-state temperature under different heating environments. The different heating environments were as follows: (a) a heating power of 40 W under a

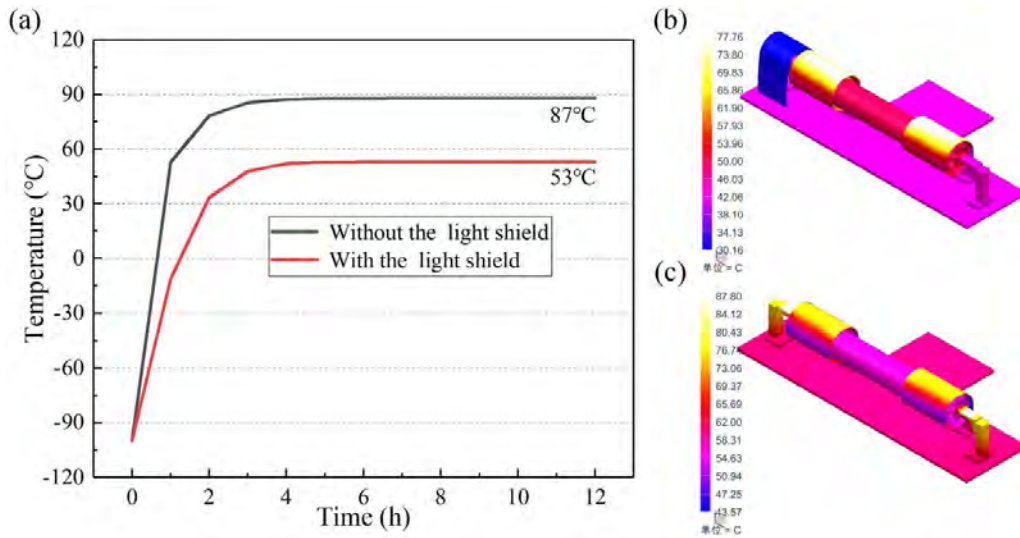


Figure 4. The surface temperature of the SMPC-FSAS before and after adding the light shield: (a) steady-state temperature of the SMPC-LL; (b) steady-state temperature distribution before adding the light shield; (c) steady-state temperature distribution after adding the light shield.

vacuum environment; (b) a convective heat transfer coefficient of $6 \text{ W (m}^2 \text{ °C)}^{-1}$ with a heating power of 40 W ; (c) a heating power of 80 W under a vacuum environment; (d) a convective heat transfer coefficient of $6 \text{ W (m}^2 \text{ °C)}^{-1}$ with a heating power of 80 W .

3.2. Numerical analysis

Figure 4(a) shows the steady-state temperature of the SMPC-LL before and after adding the light shield under the high-temperature working condition. Before the light shield was added, the highest temperature of the SMPC-LL was 87 °C , which was higher than the thermal control temperature of the SMPC-LL in the design. Satisfactorily, the highest temperature of the SMPC-LL was 53 °C after adding the light shield, which could meet the thermal control requirements. The results show that the light shield could effectively reduce the surface temperature of the SMPC-LL. Figures 4(b) and (c) present the steady-state temperature distribution of the SMPC-FSAS before and after adding the light shield, respectively. Comparing the two states, it was found that the surface temperature of the locking mechanism reduced after the addition of the light shield. The temperature of the SMPC-LL at the gap between the SMPC-LT and the light shield was higher than that at other locations. A gap of 10 mm was designed to ensure that the deployment of the SMPC-LT was not hindered.

Figure 5 illustrates the high-temperature transient-state temperature curve. The highest temperatures of SMPC-LT and SMPC-LL were 76.1 °C and 49.8 °C , respectively. The lowest temperatures of SMPC-LT and SMPC-LL were -78.1 °C and -43.2 °C , respectively. For high-temperature working conditions of the orbit for one day, the SMPC-FSAS was located in the shaded area against the sun at $0 \sim 12 \text{ h}$ and could not absorb solar energy, so the temperature was extremely low. Figure 6 outlines the steady-state temperature curves and temperature

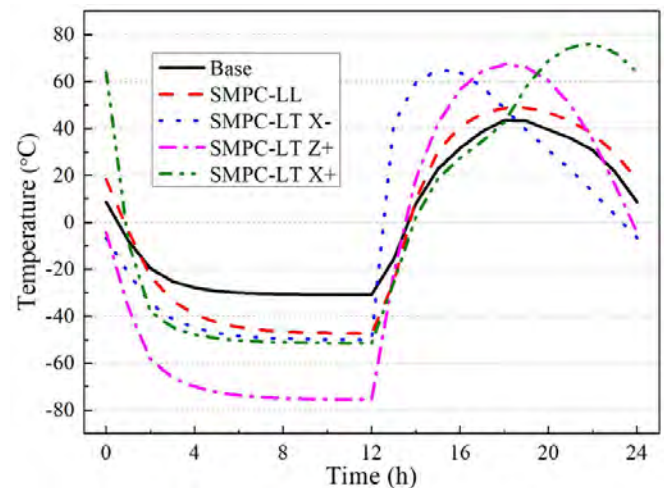


Figure 5. High-temperature transient-state temperature curve.

distributions under different working conditions. The light shield in the figure was hidden to show the temperature of the SMPC-LL. The highest steady-state temperatures of SMPC-LT and SMPC-LL were 77.8 °C and 53.1 °C respectively, and the minimum steady-state temperatures were -103 °C and -90.8 °C respectively, which are close to the heat balance temperatures. For long-term facing solar attitude, the steady-state temperatures of SMPC-LT and SMPC-LL were 59 °C and 1.3 °C , respectively.

Figures 7 and 8 show the steady-state temperature curves and temperature distributions under different heating environments. When $h_{ct} = 6 \text{ W (m}^2 \text{ °C)}^{-1}$, under heating powers of 40 W and 80 W , the steady-state temperatures of the SMPC-LT were 127.21 °C and 200.43 °C , respectively. When $h_{ct} = 0 \text{ W (m}^2 \text{ °C)}^{-1}$, under heating powers of 40 and 80 W , the steady-state temperatures of the SMPC-LT were

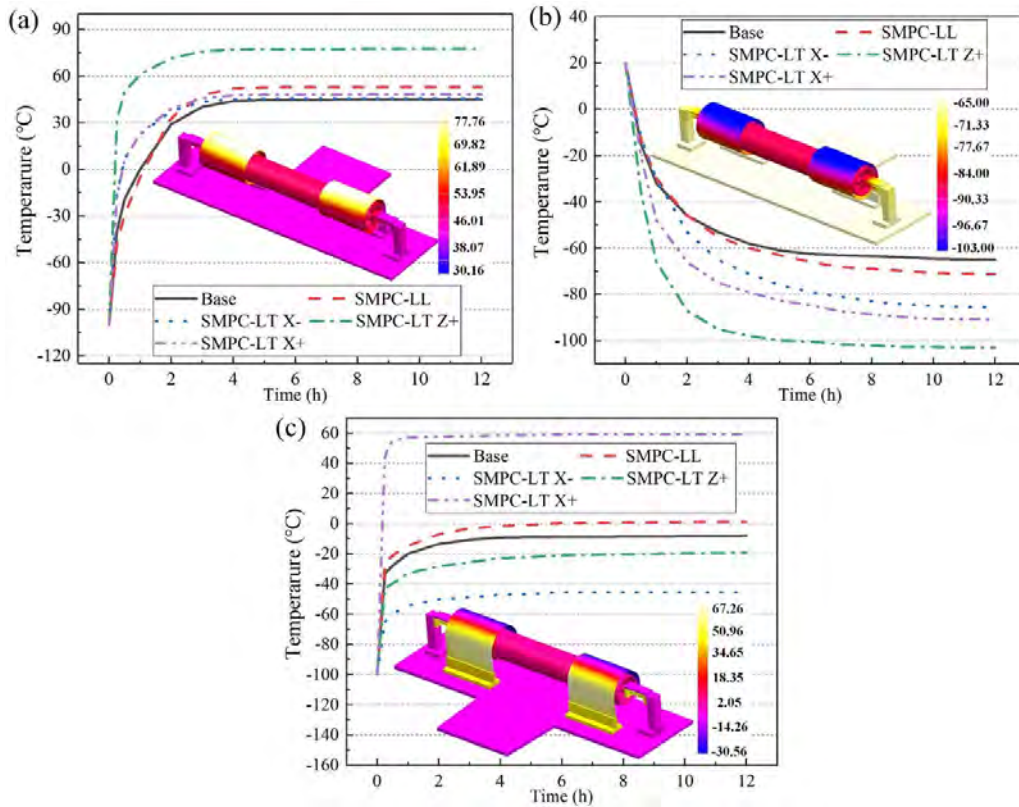


Figure 6. The steady-state temperature curves and temperature distributions under different working conditions: (a) high-temperature steady-state condition; (b) low-temperature steady-state condition; (c) long-term facing solar attitude steady-state condition.

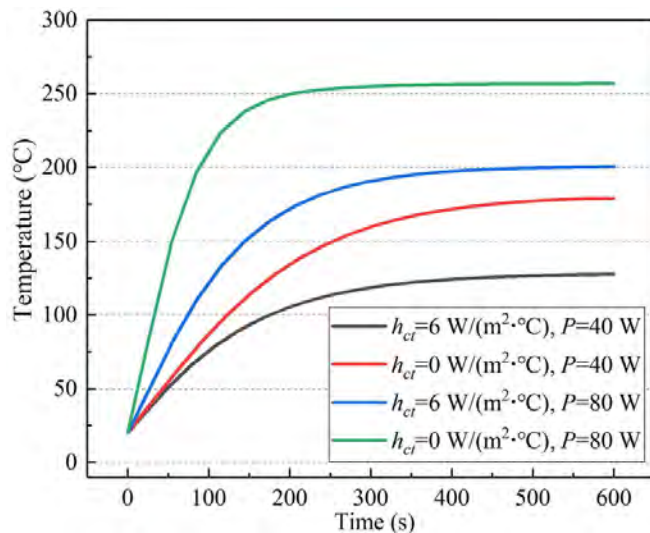


Figure 7. The steady-state temperature curve of the highest temperature point during the heating process of the SMPC-LT.

179.38 °C and 256.80 °C, respectively. It can be observed that the numerically predicted steady-state temperatures are very close to the theoretical and experimental temperatures. The results also show that the design of double circuit heating film can meet the heating power requirements under different environments.

4. Experiments

4.1. Dynamic mechanical analysis

DMA was used to measure the T_g of shape-memory materials. In this study, a dynamic thermal analyzer (NETZSCH DMA Q800) was used and the three-point bending mode was selected. The dimensions of the specimens were 35 mm (length) \times 6 mm (width) \times actual thickness for each material. During the test, the loading frequency was 1 Hz and the heating rate was 5 °C min⁻¹.

4.2. Shape fixity test

A shape fixity test of the SMPC-LL was conducted to verify the shape fixity ratio at high temperatures. An ambient temperature can stimulate the recovery of the SMPC-LL and activate the locking and release mechanism of the SMPC-FSAS. In this study, the SMPC-LLs of the storage state were placed in chambers with temperatures of 80 °C, 100 °C, and 120 °C for shape fixity tests. During the testing, the shape recovery of the SMPC-LLs was recorded every 5 d for 50 d, and then the shape fixity ratio of the SMPC-LL was calculated according to the schematic diagram (as shown in figure 9). Because the locking and release of the SMPC-FSAS are mainly determined by the distance between the two ends of the SMPC-LL, this study describes the shape change by the distance between

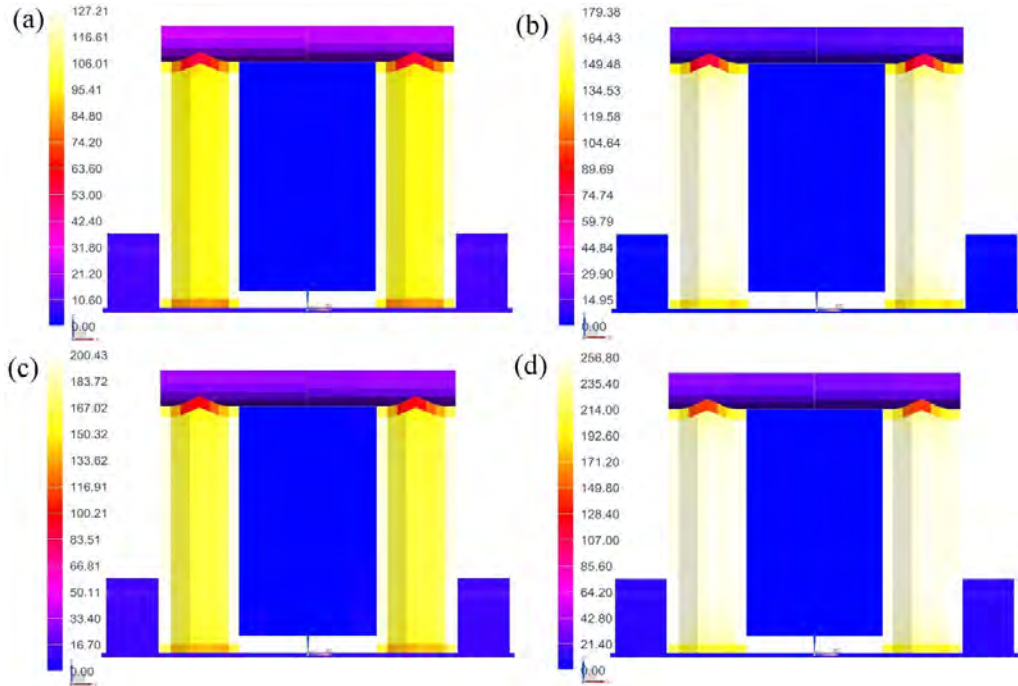


Figure 8. The steady-state temperature distributions of the SMPC-LT: (a) $h_{ct} = 6 \text{ W (m}^2 \text{ °C)}^{-1}$, $P = 40 \text{ W}$; (b) $h_{ct} = 0 \text{ W (m}^2 \text{ °C)}^{-1}$, $P = 40 \text{ W}$; (c) $h_{ct} = 6 \text{ W (m}^2 \text{ °C)}^{-1}$, $P = 80 \text{ W}$; (d) $h_{ct} = 0 \text{ W (m}^2 \text{ °C)}^{-1}$, $P = 80 \text{ W}$.

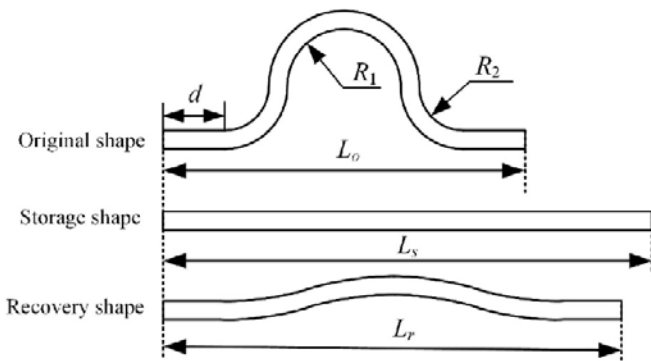


Figure 9. Schematic diagram of the shape fixity ratio test.

the two ends of the SMPC-LL. The calculation equation of the shape fixity ratio is as follows:

$$R_f = \frac{L_r - L_o}{L_s - L_o} \times 100\% \quad (8)$$

where R_f denotes the shape fixity ratio, L_r denotes the recovery length, L_o denotes the length of the original shape ($L_o = 28 \text{ mm}$), L_s denotes the length of the storage shape ($L_s = 38 \text{ mm}$), R_1 and R_2 denote the radius of the arc segment ($R_1 = R_2 = 4.39 \text{ mm}$), and d denotes the length of the linear segment ($d = 5 \text{ mm}$).

4.3. Thermal balance test

The TBT was conducted to simulate the thermal environment (vacuum, cold black) of the geosynchronous orbit to verify

the thermal balance temperature of the SMPC-FSAS. The KFTA solar simulator (as shown in figure 10(a)) developed by the Beijing Institute of Satellite Environmental Engineering was used to investigate the surface temperature variation and steady-state thermal balance temperature of the SMPC-FSAS. The device can simulate the solar radiation environment, with an irradiation volume of $\Phi 600 \times 600 \text{ mm}$ and a limit vacuum degree of $1 \times 10^{-5} \text{ Pa}$. Its radiation heat flux ranges from $707\text{--}2175 \text{ W m}^{-2}$. To evaluate and compare the thermal balance temperature, the paste position of the thermistors was consistent with that of the numerical simulation (as illustrated in figure 3). The vacuum degree was $5.9 \times 10^{-5} \text{ Pa} \sim 1.2 \times 10^{-5} \text{ Pa}$ during the test, the temperature of the cold black screen was less than -173 °C , and the satellite board simulator (as illustrated in figure 10(b)) were stable at 50 °C (high-temperature working condition) and -10 °C (low-temperature working condition). A solar simulator was used for irradiating perpendicular to the installation surface to simulate the ordinary attitude (as shown in figure 10(c)), and the solar simulator was used to irradiate parallel to the installation surface to simulate the long-term facing solar attitude (as shown in figure 10(d)). During the test, the placement state of the SMPC-FSAS was adjusted after the test at the ordinary attitude, and the long-term facing attitude test was carried out after the vacuum was exhausted again. The four working conditions in TBT were consistent with those in numerical simulation. Owing to the limitation of thermal balance equipment, the heat flow under the transient-state condition in the TBT was calculated from the different incidence angles of sunlight, while the transient-state condition in the numerical simulation was based on the actual continuous solar incidence angle.

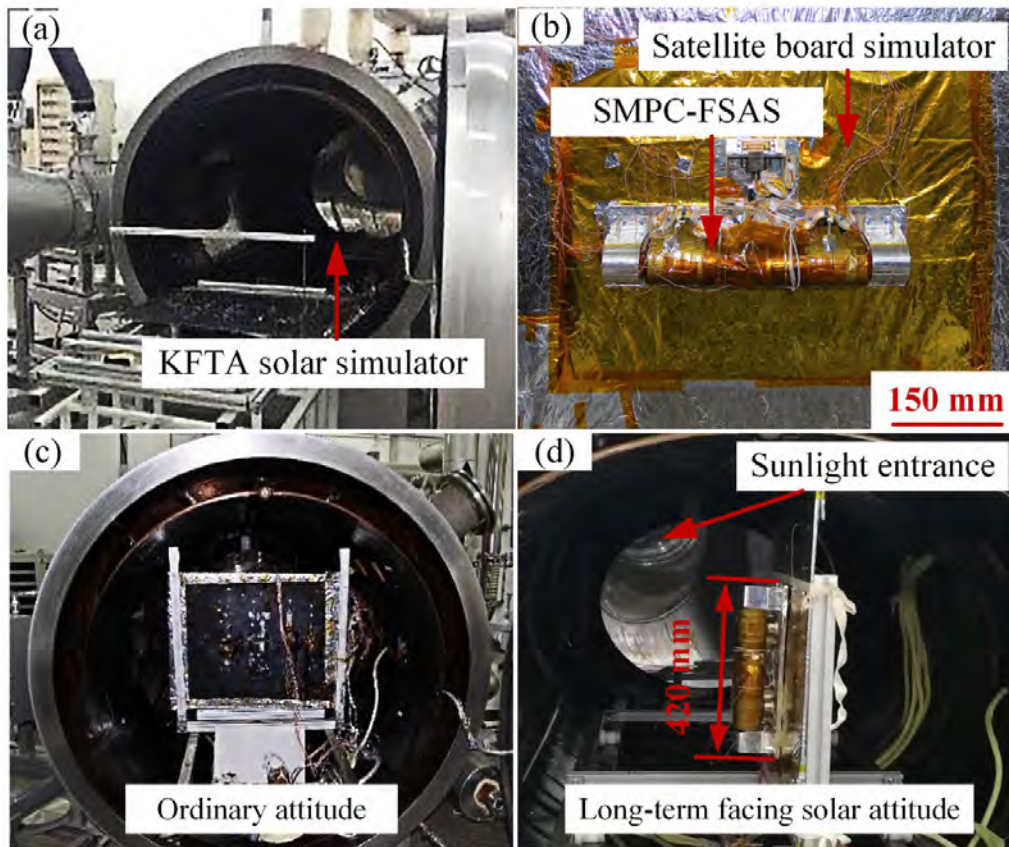


Figure 10. TBT of the SMPC-FSAS: (a) KFTA solar simulator; (b) simulated satellite board installation; (c) ordinary attitude; (d) long-term facing solar attitude [33].

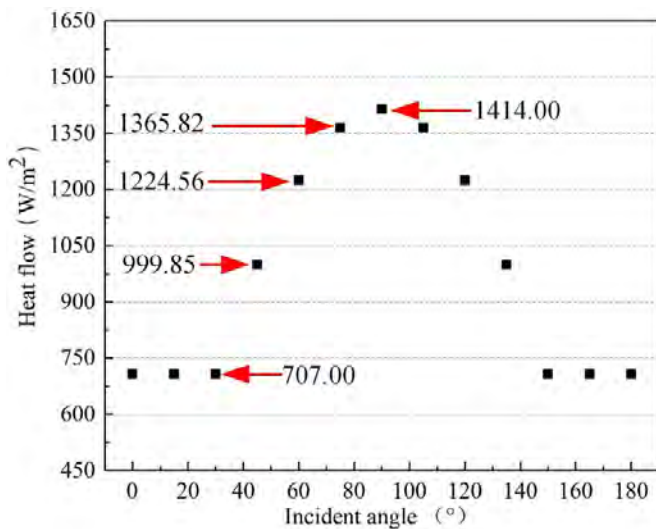


Figure 11. Heat flux corresponding to different incident angles of sunlight.

During the steady-state condition test, continuous irradiation was provided for 12 h or until a steady state was reached.

The heat flow at different incident angles was calculated as in equation (9). In this study, the incidence angle of sunlight is the angle between direct sunlight and the base of the SMPC-FSAS. Figure 11 shows the heat flux corresponding to

different incident angles of sunlight. Since the minimum heat flow of the solar simulator was 707 W m^{-2} , when the calculated heat flow was less than 707 W m^{-2} , the heat flow was input as 707 W m^{-2}

$$Q_{\theta} = Q_{\max} \times \sin \theta. \quad (9)$$

where Q_{θ} is the heat flux corresponding to the incident angle θ , Q_{\max} is the maximum heat flux ($Q_{\max} = 1414 \text{ W m}^{-2}$), and θ is the incident angle.

4.4. Thermal vacuum and thermal cycle test

To investigate the thermal stability of the SMPC-FSAS, TVT of 6.5 cycles and TCT of 18.5 cycles were performed on the SMPC-FSAS [36] (as revealed in figures 12 and 13). The TVT was carried out in the thermal vacuum chamber (KM2) developed by the Beijing Institute of Satellite Environmental Engineering. The equipment can simulate the high and low temperature environment in a vacuum environment with an effective volume of $\Phi 1700 \times 2500 \text{ mm}$. Its vacuum degree can reach $5 \times 10^{-4} \text{ Pa}$, and its temperature ranges from $-160 \text{ }^{\circ}\text{C}$ to $150 \text{ }^{\circ}\text{C}$. The TCT was carried out in the high and low temperature test chamber (F-10A) developed by the Chongqing Yinhe Testing Instrument Co., Ltd The equipment can simulate the atmospheric high and low temperature environment with an effective volume of $600 \times 600 \times 670 \text{ mm}$, and its

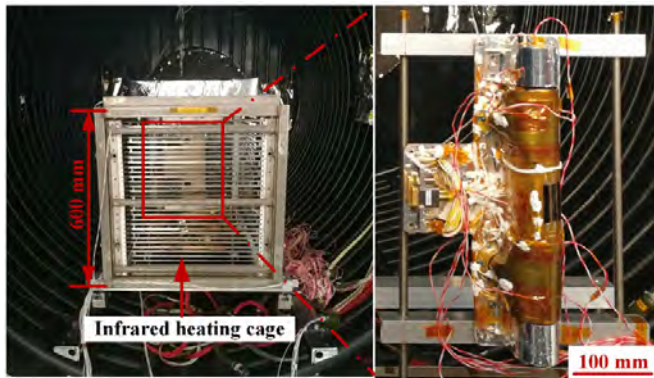


Figure 12. TWT of the SMPC-FSAS [33].

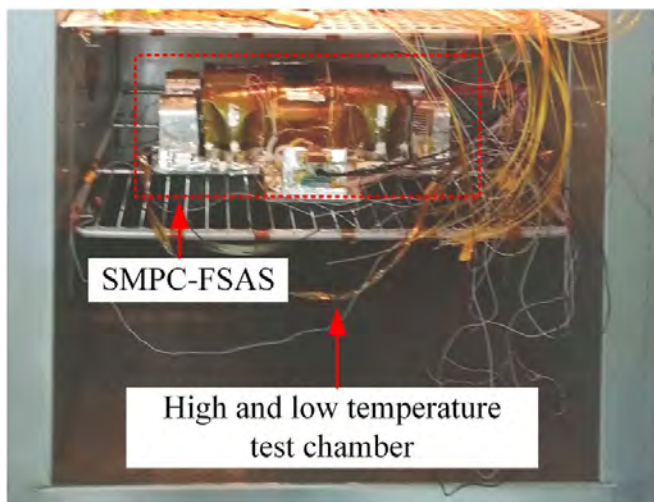


Figure 13. TCT of the SMPC-FSAS [33].

temperature ranges from $-150\text{ }^{\circ}\text{C}$ to $180\text{ }^{\circ}\text{C}$. The ambient temperature of the SMPC-FSAS was controlled by using an infrared heating cage during the TWT. A temperature chamber was used to control the ambient temperature during the TCT. Considering the TBT error, the upper and lower temperature limits of the TWT and TCT were obtained by using a deviation of $15\text{ }^{\circ}\text{C}$ on the basis of the thermal balance temperature obtained by TBT. Therefore, during the TWT and TCT, the temperature range was $-117\text{ }^{\circ}\text{C} \sim 88\text{ }^{\circ}\text{C}$. For the TWT, each cycle time was 20.5 h, and the vacuum degree was less than $6.65 \times 10^{-3}\text{ Pa}$. The heating and cooling rates were 1 and $0.37\text{ }^{\circ}\text{C min}^{-1}$, respectively. In the TCT process, each cycle time was 12.3 h, and the temperature change rate was $3\text{ }^{\circ}\text{C min}^{-1}$. Once the temperature remained stable for 1 h, it was maintained in a stable state for 4 h.

4.5. Heating test

The heating test of the SMPC-LT was conducted to examine the temperature change. During the test, the ambient temperature was $20\text{ }^{\circ}\text{C}$, and the heating power of the SMPC-LT under the atmospheric environment and vacuum environment

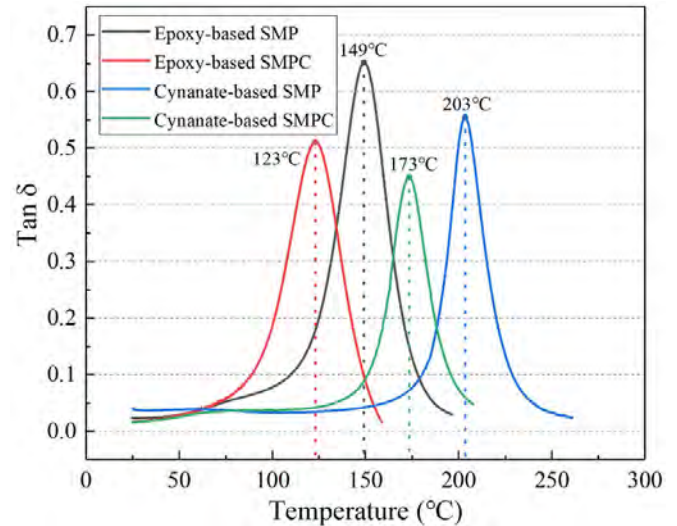


Figure 14. Tan δ curve of the shape memory materials.

was 80 W and 40 W, respectively. The vacuum degree of the vacuum environment was $6.65 \times 10^{-3}\text{ Pa}$. The test time was 600 s, and the temperature was monitored by attaching a temperature sensor to the surface of the SMPC-LT.

5. Results and discussion

5.1. Dynamic mechanical properties

The Tan δ curve of the shape memory materials is given in figure 14. The temperature corresponding to the peak of Tan δ is the T_g of the shape memory materials. It can be noted that the T_g of the epoxy-based SMP and cyanate-based SMP were $149\text{ }^{\circ}\text{C}$ and $203\text{ }^{\circ}\text{C}$, respectively. The T_g of the epoxy-based SMPC and cyanate based SMPC were reduced by $26\text{ }^{\circ}\text{C}$ and $30\text{ }^{\circ}\text{C}$ lower than that of their pure polymer forms, respectively, which was due to the addition of the carbon fiber twill. As the T_g of cyanate-based SMPC was higher than that of epoxy-based SMPC, the shape fixity ratio of cyanate-based SMPC was higher than that of epoxy-based SMPC at high temperatures. The SMPC-LL used in the SMPC-FSAS were required to maintain a superior shape fixity ratio at high temperatures. The SMPC-LTs had lower requirements for the thermal environment. Therefore, epoxy-based SMP was used as a matrix to prepare SMPC-LT.

5.2. Shape fixity performance

The shape fixity ratio of the SMPC-LL in 30 d is illustrated in figure 15. The shape fixity ratios of the SMPC-LLs at $80\text{ }^{\circ}\text{C}$, $100\text{ }^{\circ}\text{C}$, and $120\text{ }^{\circ}\text{C}$ after 50 d were approximately 100%, 99.2%, and 98.0%, respectively. Notably, SMPC-LL could be completely fixed at $80\text{ }^{\circ}\text{C}$. At temperatures of $100\text{ }^{\circ}\text{C}$ and $120\text{ }^{\circ}\text{C}$, the SMPC-LLs maintained a high shape fixity ratio, and the shape could also be completely fixed over time.

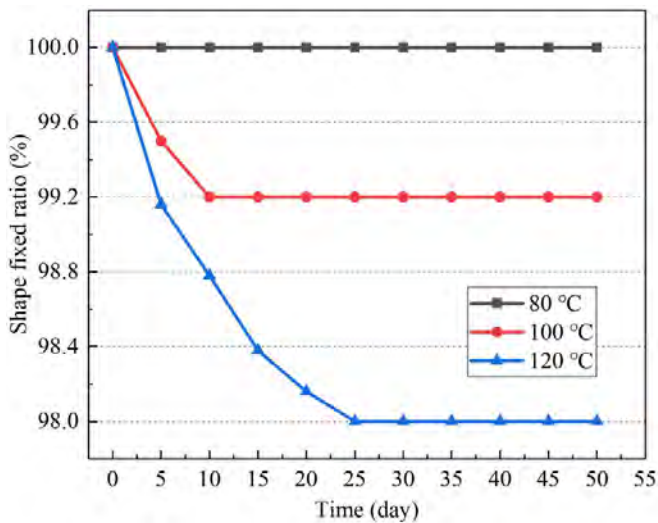


Figure 15. Shape fixity ratio of the SMPC-LL in 50 d.

5.3. Thermal balance test analysis

The high-temperature steady-state temperature curve under high temperature is shown in figure 16(a). The steady-state temperature at the Z+ position of the SMPC-LT was 73.2 °C, which was 37.4 °C and 36.2 °C higher than the temperatures at the X+ and X− positions, respectively. This is because the Z+ position of the SMPC-LT directly faces the heat flow input direction. The highest steady-state temperature would be used as the high-temperature reference value for TVT and TCT. The low-temperature steady-state temperature curve is presented in figure 16(b). The result revealed that the lowest temperature of the SMPC-LT was −102 °C, which could be used as the low-temperature reference value for the TVT and TCT. The transient-state temperature curve in ordinary attitude is outlined in figure 16(c). The components of the SMPC-FSAS demonstrated good symmetry in the low-temperature transient and high-temperature transient states. Significant differences between the transient and the steady-state temperatures were not observed. This is because of the small heat capacity of the structure. Figure 16(d) shows the steady-state temperature curve of the SMPC-FSAS in the long-term facing solar attitude. Because the X+ direction was directly facing the solar simulator, the X+ position of SMPC-LT demonstrated the highest temperature. The steady-state highest temperatures of the SMPC-LL and SMPC-LT were 2.0 °C and 61.0 °C respectively, which are safe for the shape-memory materials. Table 3 lists the comparison of surface temperature between simulation and experiment under different working conditions. Because of the simplification of the model and the limitation of the measuring point location in the experiment, minor errors were accepted. In conclusion, the simulation and experimental results were consistent with each other.

5.4. Thermal vacuum and thermal cycle test analysis

Figures 17(a) and (b) plot the temperature and time curves of the TVT and TCT, respectively. The surface temperature of

SMPC-LT was used as the control temperature. The highest temperature was 89 °C, and the lowest temperature was −120 °C during the TVT and TCT. During the TVT, the limit temperatures on the SMPC-LT surface were 83 °C and −113 °C, respectively. The temperature of the SMPC-LL was lower than that of the exposed SMPC-LT because the thermal environment was provided by the external infrared heating cage. The results comply with the test requirements. In contrast to the TVT results, the surface temperature of each component was almost the same in the TCT test curve. That is because the experimental environment for the TCT was a closed space with a relatively uniform temperature. The temperature curves of TVT and TCT in each cycle were consistent, which indicated that the test results were effective. After the test, the state of the SMPC-FSAS was normal after careful observation.

5.5. Deployment temperature

Figure 18 shows the temperature curves during the heating. The blue dots in the figure indicate the time when the SMPC is fully deployed. The deployment time of the SMPC-FSAS under atmospheric and high vacuum environments was 152 and 179 s, respectively. At this time, the temperature of the test points was 161 °C and 120 °C respectively. Because air convection does not occur in a vacuum, the surface temperature of the SMPC-LT was more even than that in the atmospheric environment, and the temperature required for deployment in a vacuum was lower than that in an atmospheric vacuum. The steady-state temperature of SMPC-LT under atmospheric and vacuum conditions was 198 °C and 170 °C, respectively. It can be noted that the experimental temperatures were relatively close to the theoretical results.

6. On-orbit demonstration

The SJ-20 geostationary satellite carrying the SMPC-FSAS was successfully launched at the Hainan Wenchang Satellite Launch Center on 27 December 2019, and the world's first SMPC-based flexible solar array was deployed on 5 January 2020 (as shown in figure 19). It can be noted that SMPC-FSAS can be deployed in 3 min, and the recovery ratio can reach almost 100%. When the recovery time was within 30 s and the temperature was approximately 60 °C, there was almost no recovery. When the temperature reached 80 °C, the SMPC-FSAS gradually recovered until it was fully deployed. Notably, the deployment process was extremely slow.

Figures 20(a) and (b) plot the temperature curves of the SMPC-FSAS on the orbit in the stowed and the deployed states, respectively. Because the thermistor range employed in the SMPC-FSAS was −50 °C to 250 °C, the temperature signal below −50 °C was not collected. The deployment test was performed the day after the satellite entered the synchronous orbit, and the temperature curve of the

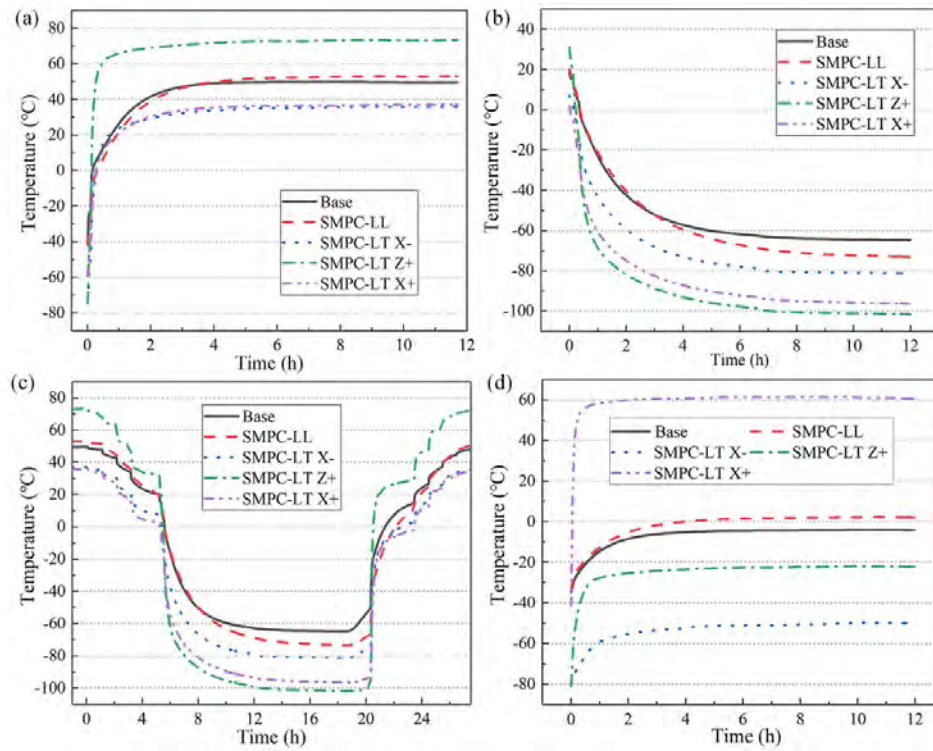


Figure 16. Temperature curve under the different conditions: (a) high-temperature steady-state condition; (b) low-temperature steady-state condition; (c) high-temperature transient-state condition; (d) long-term facing solar attitude condition.

Table 3. Comparison of steady-state temperature between simulation and experiment under the different conditions.

Condition	Method	Base	SMPC-LL	SMPC-LT X-	SMPC-LT Z+	SMPC-LT X+
High-temperature steady-state temperature	Experiment	49.6 °C	53.2 °C	35.8 °C	73.2 °C	37.0 °C
	Simulation	45.0 °C	53.1 °C	45.6 °C	77.8 °C	46.2 °C
	Relative error	-9.27%	-0.18%	27.37%	6.28%	24.86%
Low-temperature steady-state temperature	Experiment	-64.2 °C	-73.4 °C	-81.2 °C	-101.9 °C	-96.7 °C
	Simulation	-65.0 °C	-71.2 °C	-85.6 °C	-103.0 °C	-90.8 °C
	Relative error	1.25%	-2.99%	5.42%	1.08%	-6.10%
Long-term facing solar attitude steady-state temperature	Experiment	-4.8 °C	2.0 °C	-50.0 °C	-21.6 °C	61.0 °C
	Simulation	-7.1 °C	1.6 °C	-45.6 °C	-19.2 °C	59.0 °C
	Relative error	47.9%	-20%	-8.8%	-11.1%	3.28%

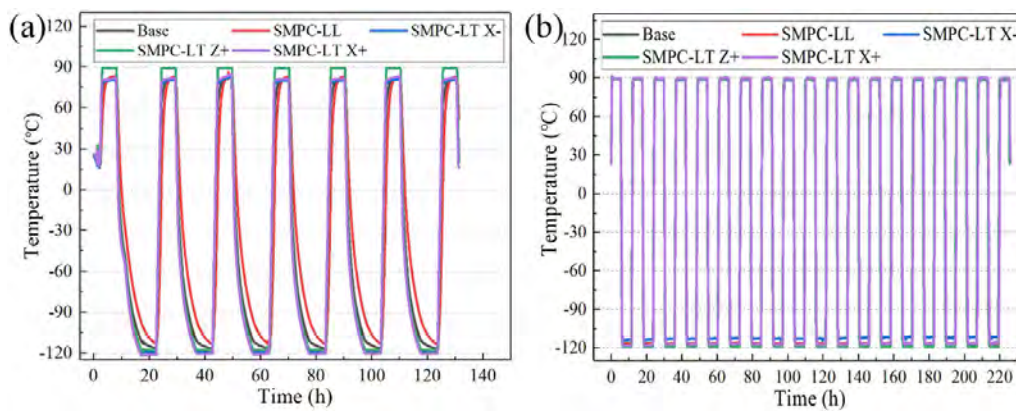


Figure 17. Temperature and time curve: (a) TVT; (b)TCT.

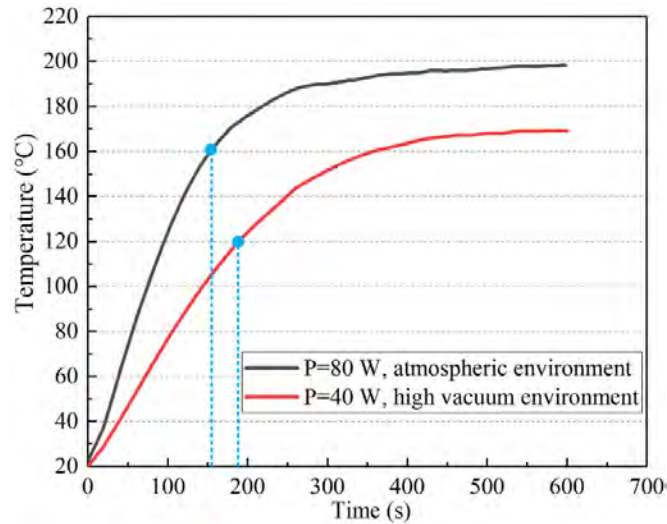


Figure 18. Temperature curve of the SMPC-LT during heating.

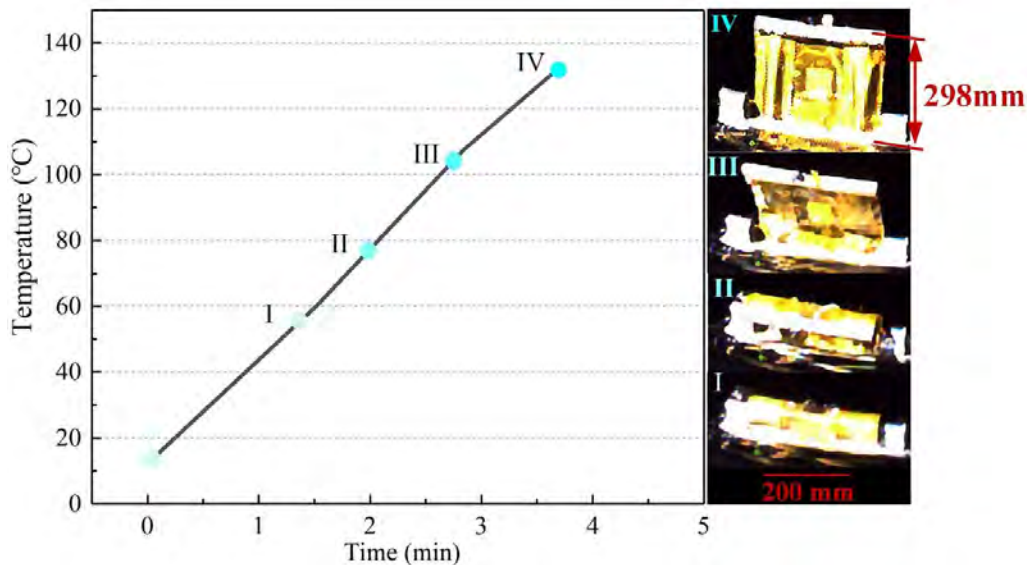


Figure 19. On-orbit temperature curve and performance demonstration of the SMPC-FSAS [33].

SMPC-FSAS in the stowed state was selected as the temperature closest to the one day on the synchronous orbit. The highest transient-state temperatures of SMPC-LL and SMPC-LT were 54.3 °C and 80.7 °C, respectively. The temperature curve of the structure on the day of deployment is shown in figure 20(c). The temperatures of the SMPC-LL and SMPC-LT increased sharply during the heating process. When the temperature was restored, the temperature curve of the structure surface was basically the same as the curve in figure 20(b). Figure 20(d) illustrates the temperature curve during deployment. The highest temperature of the SMPC-LL and the SMPC-LT during heating were 175 °C and 128 °C, respectively. The first peak in the curve for the SMPC-LL was

due to the trial power-on test, and the second peak was due to the release of the SMPC-LL. The first peak on the SMPC-LT temperature curve was caused by heating the SMPC-LT, and the second peak in the SMPC-LT temperature curve was caused by heating some additional components on the SMPC-FSAS.

The comparison of the transient-state temperature of simulation, experiment and on-orbit data is listed in table 4. The three results had a good consistency, indicating the validity of the numerical model and experimental settings. Considering the simplification of the numerical model and the location bias of the temperature sensor in the experiment, the error can be accepted.

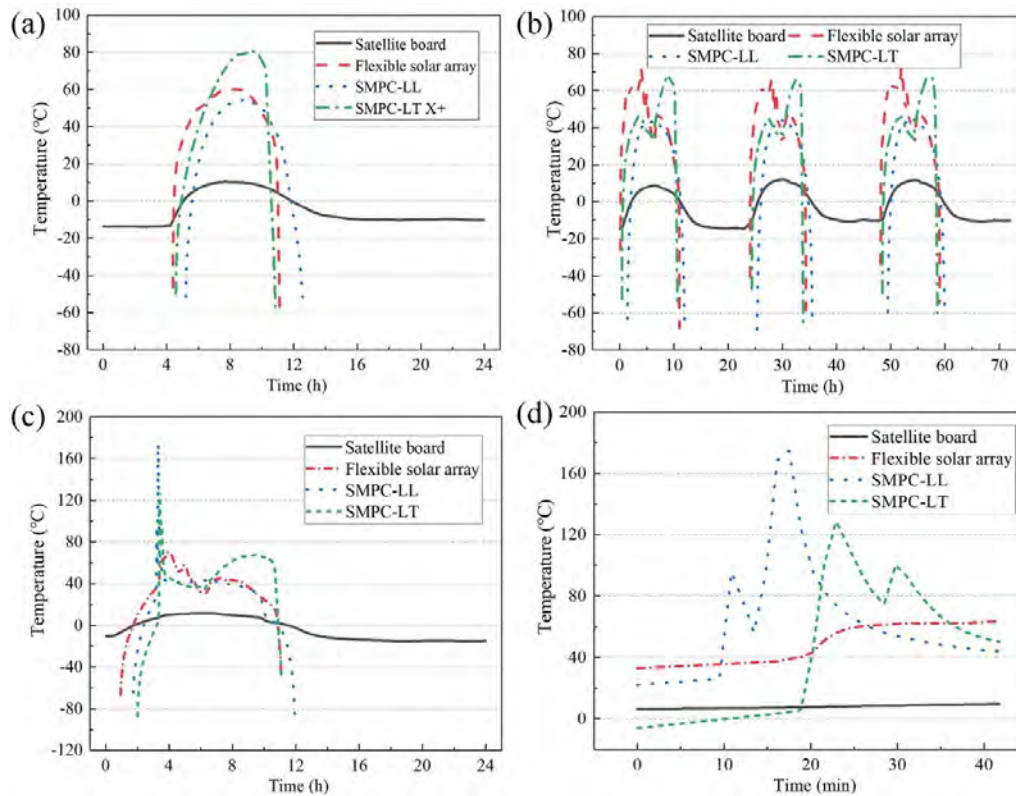


Figure 20. Temperature curve of the SMPC-FSAS on orbit: (a) stowed state; (b) deployed state; (c) temperature curve on the day of deployment; (d) temperature curve during deployment.

Table 4. Comparison of the highest transient-state temperature among simulation, experiment and on-orbit data in the stowed state (The contents in brackets are relative errors).

Method	SMPC-LL	SMPC-LT X+
On-orbit data (°C)	54.3	80.7
Simulation (°C)	49.8 (−8.28%)	76.1 (−5.70%)
Experiment (°C)	50.4 (−7.18%)	72.3 (−10.40%)

7. Conclusions

The SMPC-FSAS is not susceptible to the complex technical problems of traditional mechanical space deployable mechanisms. The thermal design of the SMPC-FSAS ensured satisfactory deployment power and temperature control. The shape fixity test showed that the SMPC-LL can be completely fixed in a temperature environment of 80 °C. The balance temperature of SMPC-FSAS was obtained using a TBT. A TVT of 6.5 cycles and a TCT of 18.5 cycles verified that SMPC-FSAS demonstrated good stability under high and low temperature environments. Additionally, the temperature distributions under different orbital conditions were obtained by numerical simulation. The highest temperatures of the SMPC-LL and SMPC-LT were 53.1 °C and 77.7 °C respectively, which met the requirements for thermal control of shape memory materials. The theoretical, simulation and experimental results

showed that the design of double circuit heating film could meet the temperature requirements of vacuum environment and atmospheric environment at the same time. The orbital data verified the correctness of the numerical model and experimental settings. On the basis of the research in this work, further research on ultra-large SMPC-FSAS will be conducted in the future.



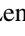
Data availability statement

All data that support the findings of this study are included within the article (and any supplementary files).

Acknowledgments

The authors are grateful for the guidance and help from the Institute of Telecommunication Satellite, China Academy of Space Technology (CAST). The authors would like to acknowledge the support from Shanghai Space Power Institute who has specially developed the flexible blanket solar array for the SMPC-FSAS project. The authors would like to thank Fenghua Zhang, Linlin Wang and Yongdie Deng for their help in the preparation and characterization of materials. This work is supported by the National Natural Science Foundation of China (Grant Nos. 11632005, 11872020).

ORCID iDs

Sida Hao  <https://orcid.org/0000-0001-7264-1550>
 Yanju Liu  <https://orcid.org/0000-0001-8269-1594>
 Jinsong Leng  <https://orcid.org/0000-0001-5098-9871>

References

- [1] Fang Y *et al* 2017 Reconfigurable photonic crystals enabled by multistimuli-responsive shape memory polymers possessing room temperature shape processability *ACS Appl. Mater. Interfaces* **9** 5457–67
- [2] Guo Y, Lv Z, Huo Y, Sun L, Chen S, Liu Z, He C, Bi X, Fan X and You Z 2019 A biodegradable functional water-responsive shape memory polymer for biomedical applications *J. Mater. Chem. B* **7** 123–32
- [3] Hassanzadeh-Aghdam M K, Ansari R and Mahmoodi M J 2019 Thermo-mechanical properties of shape memory polymer nanocomposites reinforced by carbon nanotubes *Mech. Mater.* **129** 80–98
- [4] Li M, Chen J, Shi M, Zhang H, Ma P X and Guo B 2019 Electroactive anti-oxidant polyurethane elastomers with shape memory property as non-adherent wound dressing to enhance wound healing *Chem. Eng. J.* **375** 121999
- [5] Roth P J and Lowe A B 2017 Stimulus-responsive polymers *Polym. Chem.* **8** 10–11
- [6] Liu T *et al* 2017 Stimulus methods of multi-functional shape memory polymer nanocomposites: a review *Composites A* **100** 20–30
- [7] Zhao W, Liu L, Zhang F, Leng J and Liu Y 2019 Shape memory polymers and their composites in biomedical applications *Mater. Sci. Eng. C* **97** 864–83
- [8] Pilate F, Toncheva A, Dubois P and Raquez J-M 2016 Shape-memory polymers for multiple applications in the materials world *Eur. Polym. J.* **80** 268–94
- [9] Liu Y, Du H, Liu L and Leng J 2014 Shape memory polymers and their composites in aerospace applications: a review *Smart Mater. Struct.* **23** 023001
- [10] Liu Y, Guo Y, Zhao J, Chen X, Zhang H, Hu G, Yu X and Zhang Z 2019 Carbon fiber reinforced shape memory epoxy composites with superior mechanical performances *Compos. Sci. Technol.* **177** 49–56
- [11] Li Z, Hu J, Ma L and Liu H 2020 Shape memory CTBN/epoxy resin/cyanate ester ternary resin and their carbon fiber reinforced composites *J. Appl. Polym. Sci.* **137** 48756
- [12] Zeng H, Liu J, Xie Z and Sun H 2019 Modeling the shape memory and strength properties of fiber-reinforced shape memory polymer composite laminates *Smart Mater. Struct.* **28** 105011
- [13] Yu K, Liu Y, Liu Y, Peng H-X and Leng J 2014 Mechanical and shape recovery properties of shape memory polymer composite embedded with cup-stacked carbon nanotubes *J. Intell. Mater. Syst. Struct.* **25** 1264–75
- [14] Goda I, Zubair Z, L'Hostis G and Drean J-Y 2020 Design and characterization of 3D multilayer woven reinforcements shape memory polymer composites *J. Compos. Mater.* **55** 653–73
- [15] Chatterjee T, Dey P, Nando G B and Naskar K 2015 Thermo-responsive shape memory polymer blends based on alpha olefin and ethylene propylene diene rubber *Polymer* **78** 180–92
- [16] Cheng Y, Bian L, Wang Y and Taheri F 2014 Influences of reinforcing particle and interface bonding strength on material properties of Mg/nano-particle composites *Int. J. Eng. Sci.* **51** 3168–76
- [17] Sun Y-C, Chu M, Huang M, Hegazi O and Naguib H E 2019 Hybrid electroactive shape memory polymer composites with room temperature deformability *Macromol. Mater. Eng.* **304** 1900196
- [18] Lewis C L and Dell E M 2016 A review of shape memory polymers bearing reversible binding groups *J. Polym. Sci. B* **54** 1340–64
- [19] Chamberlain M K, Kiefer S H, LaPointe M and LaCorte P 2021 On-orbit flight testing of the roll-out solar array *Acta Astronaut.* **179** 407–14
- [20] Schenk M, Viquerat A D, Seffen K A and Guest S D 2014 Review of inflatable booms for deployable space structures: packing and rigidization *J. Spacecr. Rockets* **51** 762–78
- [21] Johnson L, Young R M and Montgomery I E E 2007 Recent advances in solar sail propulsion systems at NASA *Acta Astronaut.* **61** 376–82
- [22] Zhang R, Guo X, Liu Y and Leng J 2014 Theoretical analysis and experiments of a space deployable truss structure *Compos. Struct.* **112** 226–30
- [23] Li F, Liu Y and Leng J 2019 Progress of shape memory polymers and their composites in aerospace applications *Smart Mater. Struct.* **28** 103003
- [24] Sokolowski W M and Tan S C 2007 Advanced self-deployable structures for space applications *J. Spacecr. Rockets* **44** 750–4
- [25] Liu Z, Li Q, Bian W, Lan X, Liu Y and Leng J 2019 Preliminary test and analysis of an ultralight lenticular tube based on shape memory polymer composites *Compos. Struct.* **223** 110936
- [26] Aoki T, Higuchi K and Watanabe K 2014 Progress report of simple space experiment project on ISS Japan experiment module *Trans. Japan Soc. Aeronaut. Space* **12** Tc_1–Tc_6
- [27] Leng J, Xie F, Wu X and Liu Y 2014 Effect of the γ -radiation on the properties of epoxy-based shape memory polymers *J. Intell. Mater. Syst. Struct.* **25** 1256–63
- [28] Tan Q, Li F, Liu L, Liu Y, Yan X and Leng J 2019 Study of low earth orbit ultraviolet radiation and vacuum thermal cycling environment effects on epoxy-based shape memory polymer *J. Intell. Mater. Syst. Struct.* **30** 2688–96
- [29] Xie F, Liu L, Gong X, Huang L, Leng J and Liu Y 2017 Effects of accelerated aging on thermal, mechanical and shape memory properties of cyanate-based shape memory polymer: i vacuum ultraviolet radiation *Polym. Degrad. Stab.* **138** 91–97
- [30] Xu B, Fu Y Q, Ahmad M, Luo J K, Huang W M, Kraft A, Reuben R, Pei Y T, Chen Z G and De Hosson J T M 2010 Thermo-mechanical properties of polystyrene-based shape memory nanocomposites *J. Mater. Chem.* **20** 3442–8
- [31] Xu B, Fu Y Q, Huang W M, Pei Y T, Chen Z G, De Hosson J T M, Kraft A and Reuben R L 2010 Thermal-mechanical properties of polyurethane-clay shape memory polymer nanocomposites *Polymers* **2** 31–39
- [32] Lei M, Xu B, Pei Y, Lu H and Fu Y Q 2016 Micro-mechanics of nanostructured carbon/shape memory polymer hybrid thin film *Soft Matter* **12** 106–14
- [33] Lan X *et al* 2020 World's first spaceflight on-orbit demonstration of a flexible solar array system based on shape memory polymer composites *Sci. China Technol. Sci.* **63** 1436–51
- [34] Giddings S B 2016 Hawking radiation, the Stefan–Boltzmann law, and unitarization *Phys. Lett. B* **754** 39–42
- [35] Feng W, Ding Y, Yan D, Liu X, Wang W and Li D 2009 Combined low-energy environment stimulation test of geosynchronous satellite thermal control coatings *J. Spacecr. Rockets* **46** 11–14
- [36] Wang C 2018 Experimental study on thermal environment of aerospace electronic products *Shandong Ind. Technol.* **3** 51–52